Far-infrared absorber based on standing-wave resonances in metal-dielectric-metal cavity

Janardan Nath,[1] Sushrut Modak,[2] Imen Rezadad,[1] Deep Panjwani,[1] Farnood Rezaie,[1] Justin W. Cleary[3], and Robert E. Peale[1,*]

[1]Department of Physics, University of Central Florida, Orlando, Florida 32816, USA
[2]College of Optics and Photonics (CREOL), University of Central Florida, Orlando, Florida 32816, USA
[3]Air Force Research Laboratory, Sensors Directorate, Wright-Patterson Air Force Base, Ohio, 45433, USA
[*]Robert.Peale@ucf.edu

Abstract: Thin-film resonant absorbers for the far-IR spectral range were fabricated, characterized, and modeled. The 3-μm-thick structure comprises a periodic surface array of metal squares, a dielectric spacer and a metallic ground plane. Up to 95% absorption for the fundamental band at ~53.5μm wavelength (5.6 THz) is achieved experimentally. Absorption bands are independent of the structure period and only weakly dependent on polarization and incident angle. The results are well explained in terms of standing-wave resonances within individual metal-dielectric-metal cavities. The structure has application as a wavelength selective coating for far-IR bolometers.

©2015 Optical Society of America

References and links

1. R. M. Woodward, B. E. Cole, V. P. Wallace, R. J. Pye, D. D. Arnone, E. H. Linfield, and M. Pepper, "Terahertz pulse imaging in reflection geometry of human skin cancer and skin tissue," Phys. Med. Biol. **47**(21), 3853–3863 (2002).
2. J. W. Waters, L. Froidevaux, R. S. Harwood, R. F. Jarnot, H. M. Pickett, W. G. Read, P. H. Siegel, R. E. Cofield, M. J. Filipiak, and D. A. Flower, "The Earth observing system microwave limb sounder (EOS MLS) on the Aura satellite," IEEE Trans. Geo. Rem. Sens. **44**(5), 1075–1092 (2006).
3. R. Appleby and H. B. Wallace, "Standoff detection of weapons and contraband in the 100 GHz to 1 THz region," IEEE Trans. Antenn. Propag. **55**(11), 2944–2956 (2007).
4. N. Nagai, M. Sumitomo, M. Imaizumi, and R. Fukasawa, "Characterization of electron-or proton-irradiated Si space solar cells by THz spectroscopy," Semicond. Sci. Technol. **21**(2), 201–209 (2006).
5. M. Tonouchi, "Cutting-edge terahertz technology," Nat. Photonics **1**(2), 97–105 (2007).
6. G. L. Pilbratt, J. R. Riedinger, T. Passvogel, G. Crone, D. Doyle, U. Gageur, A. M. Heras, C. Jewell, L. Metcalfe, S. Ott, and M. Schmidt, "Herschel Space Observatory-An ESA facility for far-infrared and submillimetre astronomy," Astron. Astrophys. **518**, L1 (2010).
7. N. I. Landy, S. Sajuyigbe, J. J. Mock, D. R. Smith, and W. J. Padilla, "Perfect metamaterial absorber," Phys. Rev. Lett. **100**(20), 207402 (2008).
8. H. Tao, N. I. Landy, C. M. Bingham, X. Zhang, R. D. Averitt, and W. J. Padilla, "A metamaterial absorber for the terahertz regime: Design, fabrication and characterization," Opt. Express **16**(10), 7181–7188 (2008).
9. H. Tao, C. M. Bingham, A. C. Strikwerda, D. Pilon, D. Shrekenhamer, N. I. Landy, K. Fan, X. Zhang, W. J. Padilla, and R. D. Averitt, "Highly flexible wide angle of incidence terahertz metamaterial absorber: Design, fabrication, and characterization," Phys. Rev. B **78**(24), 241103 (2008).
10. N. Landy, C. Bingham, T. Tyler, N. Jokerst, D. Smith, and W. Padilla, "Design, theory, and measurement of a polarization-insensitive absorber for terahertz imaging," Phys. Rev. B **79**(12), 125104 (2009).
11. Q.-Y. Wen, H.-W. Zhang, Y.-S. Xie, Q.-H. Yang, and Y.-L. Liu, "Dual band terahertz metamaterial absorber: Design, fabrication, and characterization," Appl. Phys. Lett. **95**(24), 241111 (2009).
12. Y. Ma, Q. Chen, J. Grant, S. C. Saha, A. Khalid, and D. R. Cumming, "A terahertz polarization insensitive dual band metamaterial absorber," Opt. Lett. **36**(6), 945–947 (2011).
13. J. Grant, Y. Ma, S. Saha, A. Khalid, and D. R. Cumming, "Polarization insensitive, broadband terahertz metamaterial absorber," Opt. Lett. **36**(17), 3476–3478 (2011).
14. Y. Q. Ye, Y. Jin, and S. He, "Omnidirectional, polarization-insensitive and broadband thin absorber in the terahertz regime," J. Opt. Soc. Am. B **27**(3), 498–504 (2010).

15. M. P. Hokmabadi, D. S. Wilbert, P. Kung, and S. M. Kim, "Design and analysis of perfect terahertz metamaterial absorber by a novel dynamic circuit model," Opt. Express **21**(14), 16455–16465 (2013).
16. Q. Y. Wen, Y. S. Xie, H. W. Zhang, Q. H. Yang, Y. X. Li, and Y. L. Liu, "Transmission line model and fields analysis of metamaterial absorber in the terahertz band," Opt. Express **17**(22), 20256–20265 (2009).
17. M. Diem, T. Koschny, and C. M. Soukoulis, "Wide-angle perfect absorber/thermal emitter in the terahertz regime," Phys. Rev. B **79**(3), 033101 (2009).
18. J. Hao, L. Zhou, and M. Qiu, "Nearly total absorption of light and heat generation by plasmonic metamaterials," Phys. Rev. B **83**(16), 165107 (2011).
19. J. M. Hao, J. Wang, X. L. Liu, W. J. Padilla, L. Zhou, and M. Qiu, "High performance optical absorber based on a plasmonic metamaterial," Appl. Phys. Lett. **96**(25), 251104 (2010).
20. J. Hendrickson, J. Guo, B. Zhang, W. Buchwald, and R. Soref, "Wideband perfect light absorber at midwave infrared using multiplexed metal structures," Opt. Lett. **37**(3), 371–373 (2012).
21. J. Nath, D. Maukonen, E. Smith, P. Figueiredo, G. Zummo, D. Panjwani, R. E. Peale, G. Boreman, J. W. Cleary, and K. Eyink, "Thin-film, wide-angle, design-tunable, selective absorber from near UV to far infrared," Proc. SPIE **8704**, 8041D (2013).
22. X. Wang, C. Luo, G. Hong, and X. Zhao, "Metamaterial optical refractive index sensor detected by the naked eye," Appl. Phys. Lett. **102**(9), 091902 (2013).
23. H.-T. Chen, "Interference theory of metamaterial perfect absorbers," Opt. Express **20**(7), 7165–7172 (2012).
24. X.-Y. Peng, B. Wang, S. Lai, D. H. Zhang, and J.-H. Teng, "Ultrathin multi-band planar metamaterial absorber based on standing wave resonances," Opt. Express **20**(25), 27756–27765 (2012).
25. J. Nath, D. Panjwani, M. Yesiltas, C. Hirschmugl, and R. E. Peale, "Synchrotron infra-red spectral microscopy of metal-dielectric-metal cavity metamaterial absorbers," Proc. SPIE OP101–57 (2015) (Accepted).
26. T. W. Ebbesen, H. J. Lezec, H. F. Ghaemi, T. Thio, and P. A. Wolff, "Extraordinary optical transmission through sub-wavelength hole arrays," Nature **391**(6668), 667–669 (1998).
27. F. J. García de Abajo, "Light scattering by particle and hole arrays," Rev. Mod. Phys. **79**(4), 1267–1290 (2007).
28. B. Ung and Y. Sheng, "Optical surface waves over metallo-dielectric nanostructures: Sommerfeld integrals revisited," Opt. Express **16**(12), 9073–9086 (2008).
29. M. W. Maqsood, R. Mehfuz, and K. J. Chau, "High-throughput diffraction-assisted surface-plasmon-polariton coupling by a super-wavelength slit," Opt. Express **18**(21), 21669–21677 (2010).
30. G. L. Pollack and D. R. Stump, *Electromagnetism* (Addison-Wesley, 2002).
31. M. A. Ordal, L. L. Long, R. J. Bell, S. E. Bell, R. R. Bell, R. W. Alexander, Jr., and C. A. Ward, "Optical Properties of the Metals Al, Co, Cu, Au, Fe, Pb, Ni, Pd, Pt, Ag, Ti, and W in the Infrared and far Infrared," Appl. Opt. **22**(7), 1099–1119 (1983).
32. P. B. Johnson and R. W. Christy, "Optical constants of the noble metals," Phys. Rev. B **6**(12), 4370–4379 (1972).
33. E. D. Palik, *Handbook of Optical Constants of Solids* (Academic, 1985).
34. R. Kitamura, L. Pilon, and M. Jonasz, "Optical constants of silica glass from extreme ultraviolet to far infrared at near room temperature," Appl. Opt. **46**(33), 8118–8133 (2007).
35. J. P. Berenger, *Perfectly Matched Layer (PML) for Computational Electromagnetic* (Morgan & Claypool, 2007).
36. L. D. Landau, J. S. Bell, M. J. Kearsley, and L. P. Pitaevskii, E. M. Lifshitz, and J. B. Sykes, *Electrodynamics of Continuous Media* (Elsevier, 1984).
37. A. Hessel and A. A. Oliner, "A new theory of Wood's anomalies on optical gratings," Appl. Opt. **4**(10), 1275 (1965).
38. J. Nath, E. Smith, D. Maukonen, and R. E. Peale, "Optical Salisbury screen with design-tunable resonant absorption bands," J. Appl. Phys. **115**(19), 193103 (2014).
39. R. Peale, H. Saxena, W. Buchwald, G. Aizin, A. Muravjov, D. Veksler, N. Pala, X. Hu, R. Gaska, and M. Shur, "Grating-gate tunable plasmon absorption in InP and GaN basedHEMTs," Proc. SPIE **7467**, 74670Q (2009).
40. H. Saxena, R. Peale, and W. Buchwald, "Tunable two-dimensional plasmon resonances in an ingaas/inp high electron mobility transistor," J. Appl. Phys. **105**(11), 113101 (2009).
41. N. N. Esfahani, C. J. Fredricksen, G. Medhi, R. Peale, J. W. Cleary, W. R. Buchwald, H. Saxena, and O. J. Edwards, "Plasmon resonance response to millimeter-waves of grating-gated InGaAs/InP HEMT," Proc. SPIE **8023**, 80230R (2011).
42. N. Nader Esfahani, R. E. Peale, W. R. Buchwald, C. J. Fredricksen, J. R. Hendrickson, and J. W. Cleary, "Millimeter-wave photo-response due to excitation of two-dimensional plasmons in InGaAs/InPhigh-electron-mobility transistors," J. Appl. Phys. **114**(3), 033105 (2013).
43. S. Shu, Z. Li, and Y. Y. Li, "Triple-layer Fabry-Perot absorber with near-perfect absorption in visible and near-infrared regime," Opt. Express **21**(21), 25307–25315 (2013).

1. Introduction

Far-infrared imaging has garnered recent interest for applications in biomedicine [1], environmental remote sensing [2], explosives detection [3], materials characterization [4,5], and astronomy [6]. Bolometric detection, in which the heat generated by far-infrared absorption is sensed, is usual in this wavelength range. Sensitivity depends on having efficient

absorbers. Confinement of the absorption to specific wavelength bands of interest improves signal-to-noise ratios.

Far-infrared metamaterial absorbers (MA)have been studied as potential absorptive coatings for bolometers because of their high performance, thinness, and selectivity [7–17]. Thin Mas have been reported with polarization independent and omnidirectional absorption bands [7–24]. Typical Mas comprise 3 layers. Aperiodically patterned metallic top layer, together with a middle dielectric spacer layer and a conducting base layer, create resonances that achieve frequency-selective absorption. Reported patterns include split ring resonators (SRR) [7–16], crosses [18], squares and rectangles [19–21]. The absorption band width, polarization dependence, and spectral line shape depend on design.

Explanations for the resonant absorption are varied. Some adopt a meta-materials approach, where permittivity and permeability describe the macroscopic electrodynamics of a surface that is spatially averaged over the sub-wavelength structures, and strong dispersion due to magnetic resonances creates a surface impedance to match that of free space [7–16].Alternative descriptions exist, such as the interference approach [23], which assumes the two metal layers are linked by multiple reflections and superposition similar to Fabry-Perot resonances. The inspiration for the model we develop here is based on planar waveguides with resonant standing waves [24].

We present results for a far-IR absorber with a surface pattern comprising a periodic pattern of squares, which follows known near- [18,19], and mid-IR designs [20].There are few prior reports of periodic square (or rectangular patterns)designed for far-IR absorption beyond ~10 micron wavelengths [14,21].We observe multiple absorption bands, which are attributed to fundamental and harmonic resonances. Up to 95% absorption was achieved in the fundamental band at 53.5μm wavelength. A strong harmonic band with 98% absorption occurs at 30 μm. The absorption bands are only weakly dependent on polarization and incident angle.

To interpret the experimental far-infrared reflectivity spectra, we adapted a model proposed by Peng et al. [24], based on standing wave resonances in a finite metal-dielectric-metal (MDM)waveguide. A number of modifications were implemented to improve the accuracy of this theory. Successes of the model include prediction of the fundamental and higher order resonance wavelengths, the dependence of these resonances on square size and dielectric thickness, the independence of the resonances on the period of the structure, and the insensitivity to polarization or incidence angle. Finite difference time domain (FDTD) simulations support the interpretation.

2. Theory

Figure 1 presents a schematic side view of one unit cell of the structure. For simplicity we consider a 2D model with translational invariance normal to the plane of the figure, so that the top metallization consists of metal stripes of width l separated by gaps. The stripes are supported by a thin dielectric layer of thickness t. Underlying the dielectric is an optically thick plane of metal. Success of this model requires consideration only of one unit cell, and it is independent of the period of the stripe array or the size of the gap between the stripes. Hence, Fig. 1 presents a schematic of just a single unit cell. Far-infrared radiation incident from above, and polarized with the electric field in the plane of the figure (transverse magnetic TM), drives a periodic polarization along the top surface of the metal stripe. When the thickness of the stripe exceeds the electromagnetic penetration depth, an opposite polarization appears along the bottom surface. The fields due to this polarization are strongly intensified at the edges and corners of the stripes, creating vertically-oriented oscillating edge dipoles. These polarized edges comprise line-dipole sources of radiation, as suggested by the sketched dipolar field lines. This interpretation of the polarization and resulting field distribution was informed by the electrodynamics simulations of [24], and those shown below.
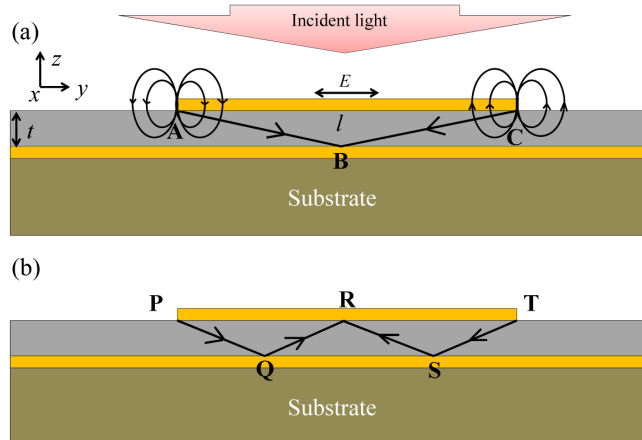
Fig. 1. Schematics of one unit cell of the structure. The edges of the metal stripes are line sources of radiation induced by the incident wave. Standing waves are formed under the stripe with different odd numbers b of reflections from the metal. Shown are rays for $b = 1$ (a) and $b = 3$ (b). Resonances correspond to odd integer numbers of half-wavelengths along the indicated paths.

That the width of the gaps between neighboring stripes is unimportant is supported by agreement of the theory with our reflectivity experiments on a single metal feature, where there are only edges while gaps are infinite [25]. In experiments reported here, the gaps are just a few microns wide, i.e. much smaller than the incident wavelengths. Nevertheless, the radiating edge dipoles assure that electromagnetic energy will appear in the dielectric layer. Existence proof of such an effect is the phenomenon of "extraordinary transmission" [26–29], through an array of sub-wavelength slits.

For our structures, the fundamental absorption resonance occurs at a wavelength (~54 μm) that is much larger than the lateral dimension l (~12 μm). The thickness of the dielectric (1-5 μm) in all our structures is also much less than the wavelength, so that we are beyond the cut-off for TM planar waveguide modes. Thus, the wave that penetrates under the squares is evanescent and should be strongly damped. However, the propagation distance required for the wave to interfere with a wave originating from the opposite edge is itself subwavelength. Thus, waves from neighboring gaps may interfere to form standing waves under the stripes. Waves at these resonances will experience extra loss due to enhanced interaction with the lossy metals.

Peng et al. [24] presented a model based on multiple reflections of rays and standing waves within similar sub-wavelength planar waveguides to interpret numerically-simulated absorption resonances. Methods based on propagation of rays, which hold in the limit of geometrical optics, are of questionable validity for subwavelength structures such as those under consideration. Nevertheless, the ray picture has known pedagogical value in understanding the modes of planar waveguides even near cutoff when the wavelength is comparable to spacing between the conducting plates [30], even though this situation is similarly outside the regime of geometrical optics. Thus, we suspend doubt until this theory can be compared with experiment below.

By symmetry, only an odd number of reflections b (for "bounces") is possible from the top and bottom metals of the waveguide. Figures 1(a) and (b) present ray diagrams that illustrate resonances with one and three bounces, respectively. The optical path lengths of the indicated resonances are different, so that we expect corresponding absorptions to occur at different wavelengths. For each closed path defined by one odd value of b, we might expect a series of harmonics corresponding to different numbers of half wavelengths between the end points.

We have assumed negligible contributions from next-nearest neighbor edges and beyond, which is reasonable considering the strong attenuation for wavelengths beyond cut-off. Thus, resonance wavelengths are expected to depend primarily on two critical cavity dimensions, namely the lateral dimension l of the stripe and the thickness of the dielectric t, but not significantly on the period (or gap dimension).In [24], Peng et al. ignored the possibility of a dependence on t by considering resonances based only on the horizontal dimension l, but predictions based on this assumption agree poorly with experiment.

For rays as indicated in Fig. 1 the optical path length is

$$\Delta = (b+1)n(\lambda)\sqrt{t^2 + l^2 / (b+1)^2} , \qquad (1)$$

Where $n(\lambda)$ is the wavelength dependent refractive index of the dielectric (SiO$_2$ in our devices), and b is the odd number of reflections. The total phase difference for rays traveling from one edge to the opposite edge, including a -πphase shift at each reflection is

$$\phi = \frac{2\pi\Delta}{\lambda} - b\pi. \qquad (2)$$

Standing-wave resonances occur when ϕ is an integral multiple m of 2π, so that the mth order standing-wave resonance occurs at wavelength

$$\lambda(b,m) = \frac{2(b+1)n(\lambda)}{b+2m}\sqrt{t^2 + l^2 / (b+1)^2} , \qquad (3)$$

Where $m = 0, 1, 2, 3....$ The number of half wavelengths along the optical path at resonance is the odd number $2m + b$. The fundamental resonance $m = 0$ for $b = 1$ is

$$\lambda(1,0) = 4n(\lambda)\sqrt{t^2 + l^2 / 4} . \qquad (4)$$

For b = 3, the fundamental $m = 0$ occurs at

$$\lambda(3,0) = \frac{8n(\lambda)}{3}\sqrt{t^2 + l^2 / 16} . \qquad (5)$$

The first harmonic $m = 1$ for $b = 1$ is

$$\lambda(1,1) = \frac{4n(\lambda)}{3}\sqrt{t^2 + l^2 / 4} . \qquad (6)$$

For the range of t and l values in our device, we anticipate the three resonances Eqs. (4)-(6) in the wavelength range of our experiment with magnitudes λ(1,0) >λ(3,0) >λ(1,1) Generally, the wavelength dependence of $n(\lambda)$ means that equations for the resonance wavelengths λ(b,m) must be solved graphically or numerically.

Since the edge polarization is the source of the waves in the waveguide, the theory predicts that the resonance wavelengths are independent of the angle of the incident light that excites the polarization.

The theory assumed translational invariance out of the plane of the page, forming a 1D grating of metal stripes, for which edge polarization can be excited only by TM polarized light. In the actual device, there are two orthogonal arrays of slits, creating a 2D array of metal squares. Thus, we expect the optical response of the actual devices to be polarization independent.

The analytic theory predicts the wavelengths of expected resonance absorptions but not the strengths or widths of the resonances. To obtain these, finite difference time domain (FDTD) electro-dynamic numerical simulations were performed using Lumerical FDTD solutions (Version 8.9). The optical constants for gold were determined from the Drude model

using with parameters from [31,32]. SiO$_2$ optical constants were taken from [33,34], for fused silica. In contrast to the analytic theory, the numerical calculations considered a fully 3D model corresponding to the actual experimental structures. The infinite array of surface squares was treated by considering a single unit cell with periodic boundary conditions in x and y directions. Perfectly matched layers (PML)–which absorb plane waves of arbitrary incidence angle, polarization, and frequency–are used to create perfectly absorbing boundary walls above and below the structure [35].These PMLs ensure that reflected and transmitted light from the sample does not return via reflection from the boundaries. A normally incident plane wave is considered with electric field polarized in y-direction, i.e. perpendicular to one set of gap edges. A frequency domain field and power monitor is used to measure the specular reflection. The reflectivity was measured using a 2D field monitor at 0 deg and spanning the unit cell. Transmittance is zero due to the metal ground plane.

The corners on the squares were not accounted for in the analytic theory. Furthermore, the numerical calculations differ from the actual devices by having perfectly sharp corners and ideal metal. These may be sources of the small disagreements between theoretical, numerical, and experimental results.

3. Experimental details

The ground plane and dielectric were deposited using a multi-pocket electron beam evaporator without breaking vacuum. First, a 10 nm Cr sticking layer followed by 200 nm of gold were deposited on glass or Si substrate. A second 10nm Cr sticking layer was then deposited followed by evaporation of the SiO$_2$ dielectric spacer. Square patterns of gold were fabricated on the SiO$_2$ film by standard photolithography, DC sputtering, and lift-off. The sputtered gold sticks well to SiO$_2$ without a sticking layer. Square dimensions and array period were determined by scanning electron microscopy (SEM). Their nominal values were 10 and 20 μm, respectively. The thickness of the top gold squares is 200 nm as determined from SEM of a cleaved and polished cross-section. This thickness is much greater than the estimated electromagnetic penetration depth of 39 μm in our wavelength range.

Reflectance was measured using a BOMEM DA8 Fourier spectrometer with globar source, 6 micron Mylar pellicle beam splitter, and room-temperature DTGS detector. Two different reflectivity accessories were used within the evacuated sample compartment. The first was at fixed angle for near-normal incidence, where the initially focused incident beam of the spectrometer was collimated by a concave mirror and was incident on the sample at an angle of 8 deg using a mirror assembly. The reflected light was diverged at the proper acceptance angle for the spectrometer's detector module. The second reflectance accessory enabled variable-angle specular reflectance measurements for incidence angles of 20, 40, and 60 deg. Reflectance R was obtained by dividing the raw reflected power spectrum with that of an optically thick smooth gold film. Transmittance through the sample is zero because the underlying gold film is optically thick. Thus, absorptance $A = 1 – R$. We assume negligible scattering because the squares are much smaller than the wavelength.

4. Results

Absorptance, $A = 1 – R$ was determined from the numerically calculated specular reflectance R as a function of geometrical parameters for the device. Figure 2(a) presents a color-map of A for square dimension $l = 11.7$ μm as a function of wavelength and dielectric thickness t, which is varied from 1 to 4 μm. Two strong absorption bands redshift with increasing t in the considered wavelength range 20 to 80 μm. The longer wave band is identified as the $\lambda(1,0)$resonance, while the shorter wave band is $\lambda(3,0)$.There is also a weak absorption band with weaker t dependence that emerges below the lowest strong band at about 25 μm, and this we identify as the $\lambda(1,1)$ resonance.
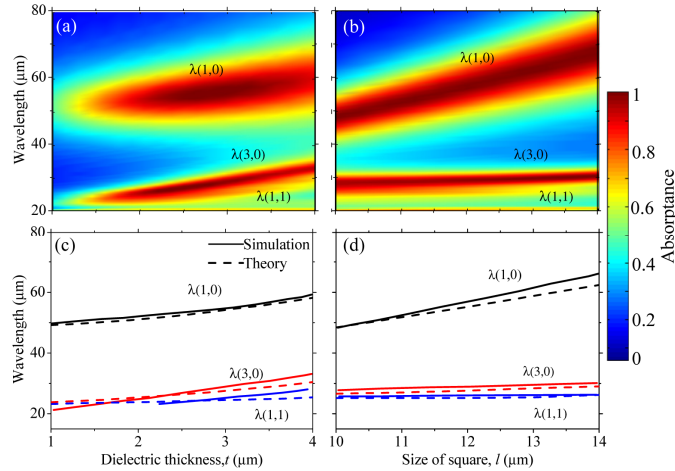
Fig. 2. Color map of absorptance as a function of wavelength and (a) dielectric thickness or (b) size of squares. Analytically- (dashed line) and numerically- (solid line) calculated resonance wavelengths as a function of (c) dielectric thickness, (d) size of squares.

Figure 2(b) presents A as a function of λ and l for $t = 3$ μm. The identification of the bands is the same as in Fig. 2(a). Comparison of the two parts of Fig. 2 shows that the dependence of $\lambda(1,0)$ on l is stronger than it is on t, but for $\lambda(3,0)$ the opposite is true. Moreover, the strengths of the absorptions are sensitive to the value of t, but not to the value of l.

Additionally, Fig. 2 shows evidence of another absorption which stays at 20 μm wavelength along the bottom edge for the complete ranges of t and l. This is attributed to secondary and coincident solutions for $\lambda(1,0)$, $\lambda(3,0)$, and $\lambda(1,1)$, which appear because of strong dispersion of SiO$_2$ near 20 microns wavelength. These identifications were determined from the graphical intersection of the refractive index spectrum (λ) for SiO$_2$ and the linear curve for $n(\lambda)$ given by Eqs. (4)-(6), as was done in [21].

Figure 2(c)-(d) compares the analytically and numerically calculated resonance wavelengths. These calculations used the same values of $n(\lambda)$ from [33,34]. The curves calculated from Eqs. (4)-(6) agree sufficiently well with the numerically-determined bands to confirm the mechanism of the absorption and the identity of the resonances. The small differences may be due to the different assumptions in the analytic and numerical calculations already mentioned.
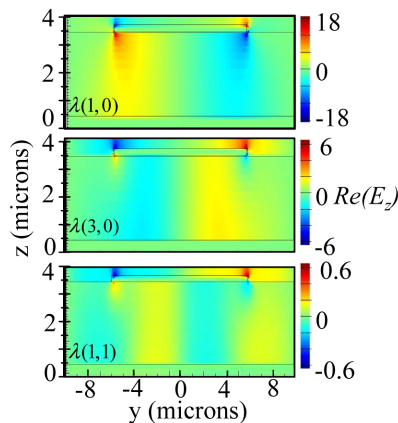

Fig. 3. $Re(E_z)$ for $\lambda(1,0)$, $\lambda(3,0)$ and $\lambda(1,1)$ of absorber with $l = 11.7$ μm and $t = 3$ μm.

Figure 3 presents color-maps of the real part of the electric field component E_z, i.e. the component normal to the plane of the device, for the $\lambda(1,0)$, $\lambda(3,0)$ and $\lambda(1,1)$ resonances. The images are side views of one period of the structure. The ground plane occupies the bottom of each frame. One of the squares appears centered horizontally near the top of the frame. The normally incident light is polarized in the plane of the figure, and this causes a polarization along the top surface of the square. Along the bottom surface, an opposite polarization appears. With charge piling up at the edges of the squares, a strong vertical polarization appears at each edge. This oscillating dipole is responsible for radiation that appears in the subwavelength cavity under the square. The plotted E_z component appears only because of this edge dipole, since the incident wave had no vertical component. A qualitatively similar picture is evident in the simulations presented by [24].

Figure 3 shows that for the $\lambda(1,0)$ resonance, E_z changes sign once in going from the left edge to the right edge, which is consistent with the observation already made that for this resonance one-half wavelength should fit along line ABC (Fig. 1).

For $\lambda(3,0)$ E_z changes sign thrice from the left edge to right, with a node at the center line, as expected if 3 half-wavelengths fit along line PQRST in Fig. 1. The regions of a particular sign of the field are unevenly distributed under the square, being highly localized near the edge and more diffuse away from the edge. Note that the color scale is reduced 3x for $\lambda(3,0)$ in comparison with $\lambda(1,0)$. Since power loss goes as the square of the field, we expect this shorter-wave absorption to be correspondingly weaker. This is confirmed in Fig. 2, where since the two strong peaks are both saturated at unity absorbance, the weaker absorption manifests as a decrease in width.
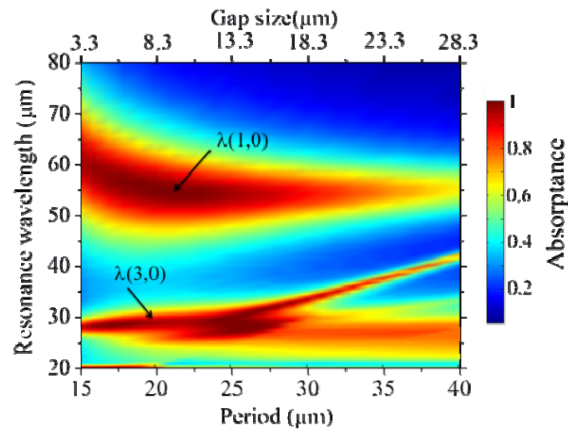

Fig. 4. Simulated absorptance as a function of wavelength and period of the squares. The size of the squares and thickness of the dielectric are l = 11.7 microns and t = 3 microns, respectively.

The color scale for $\lambda(1,1)$ is 30 x smaller than for $\lambda(1,0)$ so that this band should be much weaker than the others, in agreement with Fig. 2. In Fig. 3, considerable intensity for $\lambda(1,1)$ is found beyond the edges of the square, and it is more difficult to deduce the expected three half wavelengths between the edges. Following the horizontal centerline, E_z clearly changes sign twice, consistent with 3 half wavelengths from left to right. On the other hand, following a horizontal slice just below the square, it appears that the field changes sign 4 times, suggesting 7 half wavelengths.

The mean evolved heat density per unit time goes as $\varepsilon'' |E|^2$ [36] where the permittivity's imaginary part ε'' at the fundamental resonance in Au and SiO$_2$ has the values 44985 and 0.28, respectively [31,32]. Although E penetrates the Au only to a depth of ~40 nm, so that the volume of significant heat dissipation in Au is very small (skin effect), gold's much larger ε'' causes the total energy dissipated in the Au to exceed that in the dielectric by more than two

orders, as shown by numerical integration of simulated field distributions (e.g. Figure 3). The dissipation in top patches and ground plane is comparable. Hence, the absorption in such metal-dielectric-metal structure happens mainly in the metal. Similar conclusions were made for comparable structures designed for the near IR [18].

The analytical formulas Eqs. (4)-(6)for the resonance wavelengths are independent of the period of the surface structures. To confirm, we performed simulations as a function of period. Figure 4 presents absorptance $A = 1-R$found from the numerically calculated R for normal incidence specular reflectance as function of wavelength and period of the surface structures. The size of the squares and the thickness of the dielectric were fixed at$l = 11.7$ μm and $t = 3$ μm. Between ~20 and 40 micron period, i.e. for gaps of ~8 − 28 μm, there is no change in the position of the $\lambda(1,0)$resonance, in agreement with the analytic theory. Below 20 μm period, for gaps between squares decreasing from8 to 3 μm, the fundamental resonance red-shifts and slowly weakens. From Fig. 3, it is clear that the E_z component extends at least 2 microns beyond the edge of each square, so it is reasonable to expect that neighboring opposite dipoles begin to load and destructively interfere with each other at gaps smaller than 8 microns, thus red-shifting and weakening the resonance. Analysis of spectral line widths $\Delta\lambda$ for the fundamental from the data in Fig. 4 shows that the quality factor $Q = \lambda/\Delta\lambda$ increases from 2.7 to 5.5 as the period increases from 15 to 40 μm, presumably due to reduced interactions between unit cells. The weakening with increasing period we attribute to reduced fill-factor.

The resonance near 28 μm wavelength shows considerable structure in Fig. 4. A branch with little period dependence we identify as the $\lambda(3,0)$resonance with none of the redshift that was observed for $\lambda(1,0)$ at the smallest period, presumably due to less interaction between neighboring dipoles for these shorter-wavelength and weaker fields. At about 27 μm period, a strong feature with linear period dependence emerges and reaches ~42 μm wavelength by 40 μm period. A second weaker mode emerges near 30 μm period and reaches 33 μm wave length by 40 μm period. These two modes are interpreted as Wood's Anomalies of Rayleigh type [37], where emergence of the pth diffracted orders into the air above the grating removes intensity from the specularly reflected beam. The diffraction equation $a(\sin\theta_p − \sin\theta) = p\lambda$, with incidence angle $\theta = 0$ and diffracted angle $\theta_p = \pi/2$, gives $\lambda = a/p$, which agrees with the observed linearity of the two features and reasonably well with the observed wavelength values.
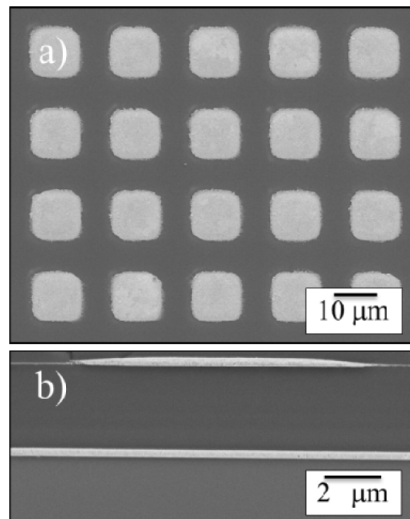

Fig. 5. SEM image of a) sample surface and b) cross-section.

The band at 20 microns wavelength, which corresponds to secondary solutions for the $\lambda(b,m)$ due to the strong dispersion of SiO_2, exists only for periods between 15 and 20 μm, before evidently blue-shifting out of the frame. This might be explained by a reduction in the effective index of the dielectric as the proportion of metal is decreased [38], which would decrease the resonance wavelength according to Eq. (4).

Figure 5 presents SEM images of a) the sample surface and b) a cleaved and polished cross-section. Such surface images were used to determine the device dimensions, which are inputs for the analytical and numerical calculations. The latter also depend on the degree to which the corners were rounded, which was also determined from the images. The cross section was used primarily to confirm the thickness of the oxide.

Figure 6 presents reflectance spectra for samples with different SiO_2 thicknesses (t). The nominally identical l values in fact vary from sample to sample by up to ~15%, due to experimental processing uncertainties such as baking time, UV light intensity, development time, etc. With increasing t the peak of the absorption shifts to longer wavelength, as predicted by Eq. (4) for the fundamental $\lambda(1,0)$. The strength of the fundamental $\lambda(1,0)$ absorption varies between 62 and 95% for the different values to t. The deepest absorption is achieved at 53.5 microns wavelength (5.6 THz) when $t = 3$ microns. This is in agreement with numerical results plotted in Fig. 2(a). The dashed line represents numerical results for $t = 3.5$ and $l = 11.7$ μm sample at normal incidence, showing good agreement with experiment.
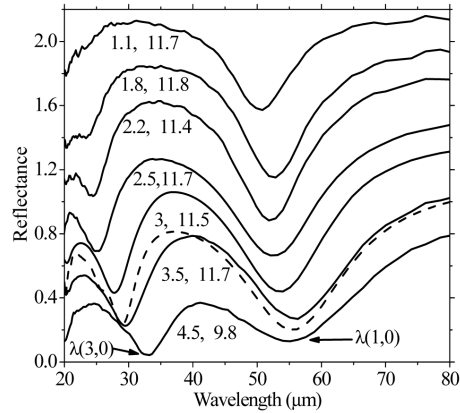

Fig. 6. Experimental reflectance spectra at 8 deg angle of incidence for different samples with numerical labels indicating SiO_2 thickness and square size, (t, l), respectively. Spectra for successively smaller t values are offset vertically by 0.2 units for clarity. The dashed line is the result of numerical calculation for structure values (3.5, 11.7) at normal incidence.

The $\lambda(3,0)$ mode emerges into the frame Fig. 6 at ~25 μm when $t = 1.8$ μm, and it redshifts finally to ~33 μm with increasing t as predicted. Evidence for the expected but weak $\lambda(1,1)$ absorption may be the asymmetry of the band due to a short-wave shoulder near 30 μm wavelength when $t = 4.5$ μm. There is evidence for the secondary solutions of $\lambda(b,m)$ due to the strong dispersion of SiO_2 at the short wave edge of the frame, as mentioned in the discussion of Fig. 2(a).

Figure 7 plots the experimental peak wavelengths of modes $\lambda(1,0)$ and $\lambda(3,0)$ from Fig. 6 as a function of theoretical resonance wavelengths according to Eqs. (4) and (5). The straight line is $\lambda(b,m) = \lambda(\exp)$. The agreement between observed resonance wavelengths and analytic theory is excellent.
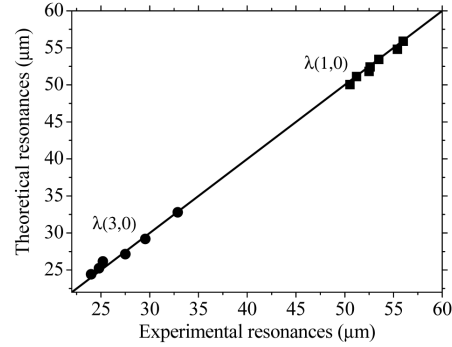
Fig. 7. Theoretical resonance wavelengths $\lambda(b,m)$ vs. experimental resonance wavelengths $\lambda(\text{exp})$ The symbols are the $\lambda(1,0)$ and $\lambda(3,0)$ experimental data for different structure dimensions l and t.

Figure 8 presents numerical absorptance spectra as a function of angle of incidence and wavelength for TM and TE light for a structure with $l = 11.7$ and $t = 3\mu$m. At normal incidence there is no distinction between TM and TE modes, and the calculated spectra are reassuringly identical. For TM polarization, the strength of the fundamental $\lambda(1,0)$ remains constant up to 70 deg angle of incidence, with the main effect being a 4% blueshift beyond 60 deg. The behavior of the $\lambda(3,0)$ band is more complicated. A strong satellite emerges at about 20 deg and redshifts linearly with angle. This is interpreted as a Wood's anomaly as discussed already in regard to Fig. 4. This is confirmed using the diffraction equation with the angle of the first diffraction mode $\theta_l = 90$, namely $\theta = \text{Arc sin}(1-\lambda/a)$. Otherwise the $\lambda(3,0)$ band shows mainly a small blue shift and intensity variation with angle.

For TE polarization, the position of the modes is almost independent of angle, and the main effect is a weakening that appears only beyond 40 deg. Interestingly, the strength of the absorption falls off much more slowly than the projected area of the square on the propagation direction ($\cos\theta$), showing that the incidence light remains effective at driving the surface polarization that leads to the edge dipoles even at large angles. The diffraction mode that appears for TM shows up only weakly in TE polarization.

Figure 9 compares experimental and numerical reflectance spectra for TM and TE polarization at angles of incidence 20, 40 and 60 degrees. Experimental data match well with simulations, particularly for the fundamental absorption at 54μm. The Wood's anomaly also appears in the experimental data, appearing most prominently in TM polarization moving from ~32 to ~38μm wavelength with increasing angle.

6. Discussion

The analytical formulas Eqs. (4)-(6) for the resonance wavelengths are independent of the period of the surface structures. For fixed square size, as the period gets smaller, the gaps become smaller. As the edges get closer, the fields from one edge dipole may begin to interact with the neighboring dipole, and since neighboring dipoles are oppositely oriented, their fields would tend to cancel. The closing of the gaps should eventually cause the absorption to disappear. As the gaps close, a weakening and red-shift are expected due to superposition of opposite dipoles and increased inertia from coupled charge oscillations. Both weakening and red-shift were observed for the fundamental $\lambda(1,0)$ with reduction in period in the numerical calculations presented in Fig. 4. However, this effect did not appear until the gaps had been reduced to just 2 microns, which is only 16% of the metal-square dimension and only 4% of the resonant wavelength.
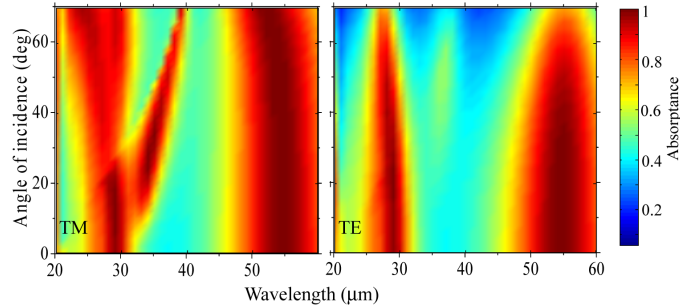
Fig. 8. Numerically calculated absorptance as a function of angle of incidence and wavelength for (a) TM and (b) TE polarization.

On the other hand, as the period is increased, different effects come into play. For periods comparable to the wavelength, diffraction orders emerge into the space above the device, taking some of the power from the specularly reflected beam, an effect known as Wood's anomaly of Rayleigh type [37]. Since both experiment and numerical calculations determine the intensity of the specularly reflected beam, these diffraction features appear in the reflectance spectrum artificially as absorptions, as in Figs. 4, 8, and 9.

For periods much larger than the square size, the absorption for wide beams would be weakened by the decrease in fill factor, but the strength of the absorption at each square should remain about the same. Indeed, diffraction-limited reflection spectral microscopy on isolated squares shows resonance wavelength and line shape to be the same, though apparently ~1.4 times weaker, than for a measurement on our periodic array with same spot size [25]. Diffraction diffuses the apparent absorption at the center of an isolated square, explaining the weakness compared to the period array as a measurement artifact.

That the absorption depends only weakly on angle of incidence is explained by the proposed mechanism, in which the incident light polarizes the squares, leading to oscillating dipoles, which are the sources of new waves that propagate into the dielectric and form lossy standing waves under the squares. The existence of such dipoles is supported by the electrodynamic simulations (Fig. 3). The standing wave model is supported by the agreement with the dependence on geometrical parameters, including dependence on the dielectric thickness, which had been previously ignored in [24].

Interestingly, the appearance of edge dipoles seems to depend on the thickness of the metal square relative to the penetration depth in that metal of the incident beam. When the penetration depth is much less than the thickness, top and underside polarizations are opposite, and edge dipoles appear, as in our case and as seen in the simulations of Peng et al. [24].But when the penetration depth is about the same as the surface-metal thickness, top and underside polarizations are the same, and no edge dipoles appear, as in the work of Hao et al. [18]. Penetration depth of electromagnetic fields is calculated at far-infrared and longer wavelengths according to the formula Sqrt[$2\rho/\mu_0\omega$] in the quasi-static approximation, where ρ is the resistivity of the metal and μ_0 is the vacuum permeability. It may be also calculated at all wavelengths from the extinction coefficient κ(imaginary part of the complex refractive index) for the metal according c/κω. At far-IR and longer wavelengths, the two formulas give the same value (~35 nm), but below far-IR wavelengths, the quasi-static approximation is inapplicable, and only the latter formula is accurate. We earlier reported an experimental investigation of the effect of top metal thickness [21]. We found no difference in the position, strength or line-width of the fundamental for Au-square thicknesses of 150 or 50 nm. However, as the thickness became comparable to (30 nm) or smaller than (10 nm) the penetration depth, the resonance significantly weakened, broadened, and blue-shifted, such that the position of the fundamental longer agreed with the resonance position predicted by Eq. (4).

We next contrast our results and interpretation with those of other authors for nominally similar absorber structures. In [18],Haoet al. present numerical results for a periodic array of Ag squares on Al_2O_3 on Ag ground plane, which are scaled to have absorption resonances at visible wavelengths. This group presented experimental demonstration of resonant absorption for one set of geometrical parameters at one angle of incidence in [19]. Notable similarities to our work include the appearance of higher order resonances, transmission through the subwavelength gaps between the squares, and standing-wave field distributions in the sub-wavelength space in the dielectric beneath the squares. A notable difference is that their calculated resonance wavelengths *increase* with decreasing dielectric thickness, opposite to our analytic, numerical, and experimental results. A hypothesis for this difference is that the visible spectral regime of [18], is closer to the plasma resonances of their metal squares, and these lie closer to the ground plane relative to their lateral dimensions. The dependence on dielectric thickness in [18], is qualitatively similar to the redshift observed in high-electron mobility transistors when the separation of between two-dimensional electron gas and the metal surface gate is decreased [39–42].A second notable difference is that Haoet al.'s simulations show no vertically-oriented oscillating edge dipoles, we attributed in the previous paragraph to the thinness of their metal squares. Our Eq. (3) gives resonance wavelengths for the structures in [18], that are a factor of ~2 too small, even when account is taken for dispersion that causes reflection phase shifts with magnitudes somewhat smaller than π in the considered spectral range. Thus, there are apparently dimensional and wavelength regimes where the standing wave model works poorly. For the dimensions and wavelengths of [18], a microscopic model based on plasmons [19], rather than standing waves may be appropriate. However, since no comparison of numerical or experimental resonance wavelengths to predictions of an analytic theory was made in [18,19], their absorption mechanism remains somewhat speculative.
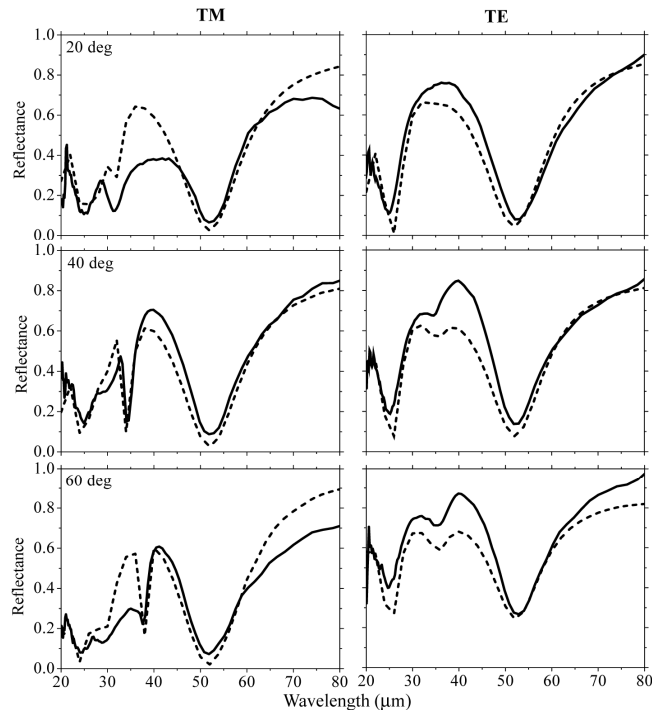

Fig. 9. Angle and polarization dependence of experimental (solid lines) and numerically calculated (dashed lines) reflectance spectra. Device parameters were $l = 11.4$ μm and $t = 2.5$ μm. Polarization is TM (left column) and TE (right column). Angle of incidence is indicated.

In [17], Diem et al. presented numerical calculations of an absorber comprising tungsten stripes on silicon nitride on tungsten ground plane. The structure is nominally similar to the model structure used for our analytic theory derivations. For the assumed dimensions, the resonance appeared at 4.28 μm in the mid-IR. As in our device all dimensions are sub-wavelength, and all the materials used are compatible with standard silicon processing. In contrast to our device, the width of their stripes was less than the gaps between them and less than the dielectric thickness. Also unlike our device, their simulated field distribution does not show standing waves under the stripes. No analytic formula is given for the resonance wavelength and no comparison to experiment is provided. Our Eq. (3) predicts the higher order resonance λ(3,0) at 4.21 μm, but the near agreement is probably coincidence given the dissimilar field distributions. Since only the magnitude of the field is given in the field distribution plot, it is impossible to know the nature of the polarization in their squares.

Chen proposed a theory based on interference between rays reflected from a periodic metal surfaced pattern and rays reflected from a metal ground plane separated by a dielectric spacer [23]. Due to the complex permittivity of the metal and dielectric, there are phase shifts on reflection and transmission that vary strongly with wavelength, allowing destructive interference between the partial front-surface reflections and multiply reflected waves in the dielectric, even though the dielectric thickness is much smaller than the wavelength. This results in a resonance with near-zero total reflectance and correspondingly strong absorption. The phase shifts and wave amplitudes needed in the Fresnel-Equation analysis were determined from numerical simulations. No analytical formula was presented to predict the resonance wavelength, which for their simulation parameters was 306 μm, and there was no comparison to experiment. Chen's model does not depend on the size of the front-surface metal features, in strong contrast to what we and others report. Chen's resonance wavelengths red-shift by about the same amount as we observe with increasing dielectric spacer thickness (10% with 4-fold change in thickness).Chen's condition for destructive interference should depend strongly on angle of incidence, which was not considered in [23], and this disagrees with the omni-directional nature of the absorption seen in Fig. 9 and widely reported by others. The mechanism proposed by Chen is similar to that used to describe Fabry-Perot type absorbers [43], such as the optical Salisbury screen [38].

In [14],Ye et al. present an LC resonance model, in which the self-inductance L for each unit cell in the periodic array is determined by the magnetic energy stored between surface structure and ground plane, and where parallel capacitors are formed between each half of the surface plate and ground plane. The resonance wavelength is proportional to the dimension of the surface structure only, but uncertainty in estimating L and C values causes the resulting analytic formula for resonance wavelength to have only order-of-magnitude accuracy when compared to experiment [21]. Furthermore, the lack of a dependence on dielectric thickness for the resonance wavelength so estimated, and the absence of higher order resonances, contradict results presented here and by others. No field distribution in cross section is presented, so it is impossible to compare the nature of the polarization in the surface structure.

The standing wave model proposed by Peng et al. [24],and elaborated here works well. The resonance wavelength depends on the dimension of the metal squares, as supported in [14,18–21,25], but not on period, at least until period becomes comparable to the square dimension enabling squares to interact. We showed that the dependence on dielectric thickness needs to be retained to obtain accurate agreement with experiment and simulation, in contrast to assumptions made by Peng et al. [24].

7. Summary

A~3-μm-thick structured film comprising an array of metal squares, a dielectric spacer, and a metallic ground plane was demonstrated to provide 95% absorption for the fundamental band at 53.5 μm wavelength, with additional resonances appearing at shorter wavelength. These bands were observed to be only weakly dependent on polarization and incident angle. The

number, center frequency, dependence on square dimension and dielectric thickness, and lack of dependence on period of the array are all well explained by a model in which the incident beam excites oscillating dipoles at the edges of the squares, which are sources for standing waves that occur in the sub-wavelength space beneath individual squares. The analytic model and physical interpretation of edge dipoles and standing waves are supported by numerical calculations, which give field visualization and spectral line shapes in agreement with experiment. These structures have application as wavelength selective coatings for far-IR bolometers.

Acknowledgment